Hindawi
Mathematical Problems in Engineering
Volume 2024, Article ID 8683229, 11 pages
https://doi.org/10.1155/2024/8683229

Research Article

Research on Nonlinear Vibration of Dual Mass Flywheel Considering Piecewise Linear Stiffness and Damping

Cuicui Wei,[1] **Hongen Niu**,[1,2] **and Liping Zeng**[3]

[1]*School of Electromechanic Engineering, Zhengzhou University of Industrial Technology, Zhengzhou 451100, China*
[2]*Engineering Technology Center of Tunnel Engineering Machinery of Henan, Zhengzhou 451100, China*
[3]*School of Mechatronics and Vehicle Engineering, East China Jiaotong University, Nanchang 330013, China*

Correspondence should be addressed to Cuicui Wei; weicuicui@zzuit.edu.cn

Received 22 February 2023; Revised 8 November 2023; Accepted 13 December 2023; Published 7 February 2024

Academic Editor: A.K. Alomari

Nonlinear torsional vibration differential equation of the nested arc-shaped short spring dual mass flywheel (DMF) is established, considering the piecewise linear stiffness and damping of the spring. The first-order approximate analytical solution under sinusoidal excitation and the amplitude–frequency characteristic function are obtained by means of the average method which verified by the Runge–Kutta (R–K) method. The effects of the parameters of input excitation, inertia, and piecewise linear stiffness and damping of DMF on the resonant amplitude, resonant frequency band, and equivalent linear natural frequency of the system are analyzed. The results show that the amplitude–frequency characteristic curve bending and jumping with the changes of excitation frequency and the peak of resonant amplitude can be obviously reduced by increasing the inertia of the primary flywheel and decreasing the inertia of the secondary flywheel. The complex nonlinear dynamic phenomena such as Period 1, quasi-periodic, and chaos are obtained by analyzing the forced vibration response under the different excitation frequencies.

1. Introduction

The torsional vibration of the engine input can be effectively attenuated through matching the DMF in the vehicle powertrain system [1–4]. The researches on the DMF have been deepened from single-stage stiffness to multistage stiffness, from linear to nonlinear.

Liu [5] established the calculation and analysis model of multi-degree-of-freedom torsional vibration system in idle state, and simplified the system into a linear system. Song et al. [6] built the torsional vibration models of vehicle powertrain matched the DMF, the effects of moment of inertia and torsional stiffness of the DMF on the inherent characteristics of the system were explored. Hou et al. [7] optimized the inertia and torsional stiffness of the DMF, and the problems of booming vibration and shift shock were solved through the verification of the actual vehicle. The above researches mainly focused on the single-stage torsional stiffness and linearity of the DMF.

With the continuous improvement of NVH quality of vehicle, the single-stage stiffness DMF can not meet the requirements better. The piecewise variable stiffness DMF, which is more and more widely used, can adjust the stiffness adaptively with the torsion angle changing [8–12]. Jiang and Chen [13] studied the design method for circumferential arc spring DMF based on a multi-mass torsional vibration model under idle and normal driving conditions. Song et al. [14] proposed the design theory of double-stage piecewise variable stiffness DMF based on friction, and studied the effect of torsional stiffness on the first and second-order resonant speed of the transmission system. Long et al. [15] studied the nonlinear vibration characteristics of circumferential long arc spring DMF with clearance angle, and explored the effect of DMF parameters on the amplitude–frequency characteristics of the system. However, the forced vibration response analysis of the system did not be further explored. Zeng et al. [16, 17] analyzed the effects of input excitation and DMF parameters on the nonlinear characteristics of a DMF powertrain by establishing a nonlinear vibration differential equation. The nonlinear forces generated by varying stiffness were considered in the study. The nonlinear factors in vibration system mainly include nonlinear stiffness and nonlinear damping. The above researches on the DMF mainly focused on the variable

stiffness, however the damping was linearized or ignored when the model built.

Wang et al. [18] studied the dynamic response of the nonlinear suspension system of the quarter truck model using the incremental harmonic balance method. Shao et al. [19] analyzed the vibratory power flow, and discussed the influence of nonlinear stiffness and damping on the power flow of vibration isolation system using the harmonic balance method. Ruan et al. [20] established the active vibration isolation system model with piecewise damping and dynamic equation and verified the correctness of the theoretical solution of the system response by the fourth-order Runge–Kutta (R–K) method. The nonlinear damping of vibration systems had been deeply studied in the literatures above, but there are few studies on the nonlinear piecewise damping of the DMF systems.

In order to improve the torque output of the DMF and match the engine with higher power and torque, the nested arc-shaped short spring DMF is studied in this paper. The nonlinear torsional vibration model of the DMF is established considering the piecewise stiffness and piecewise damping of the spring. The torsional vibration differential equation is derived by the average method. The nonlinear amplitude–frequency characteristics of the system are solved and verified by the R–K method, and the forced vibration response under different excitation frequencies of the system are analyzed. The effects of inertia and piecewise stiffness of the DMF on the amplitude–frequency characteristics and the complex nonlinear dynamic phenomena of the system are explored, and then the intrinsic nature of the nonlinear vibration characteristic of the DMF is revealed.

2. Structure and Principle of DMF

The nested arc-shaped short spring DMF with spring seats which have the function of overload protection, is mainly composed of the gear ring, primary flywheel, arc-shaped springs, spring seats, transmission flange, and secondary flywheel, as shown in Figure 1.

The primary flywheel is connected to the output end of the engine crankshaft, and the secondary flywheel is arranged on one side of the clutch. The output torque of the engine crankshaft is transferred through the damping springs which consist of inner and outer arc springs and spring seats, and the fluctuation of the output torque is reduced.

A set of arc-shaped springs consists of an internal and external arc spring as shown in Figure 2. When the relative angular of the primary and secondary flywheels is less than θ_0(θ_0—angular clearance), the torsional stiffness of the DMF depends on the first-stage stiffness k_1. When the torsion angular is greater than θ_0, the internal and external springs are connected in parallel, and the torsional stiffness of the DMF depends on the second-stage stiffness $k_2(k_2 = k_1 + k_3)$. After the spring seats contacting, the internal and external arc springs are no longer compressed to realize the overload protection of the internal and external arc springs. The piecewise linear stiffness characteristics (while $\theta > 0°$) of the DMF are shown in Figure 3.

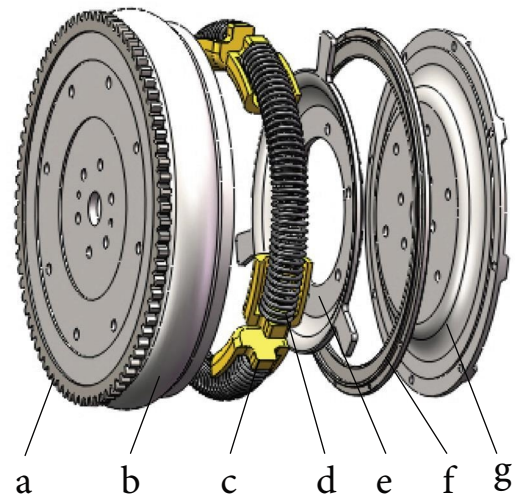

Figure 1: Schematic of the main structure of the DMF. (a) Gear ring, (b) primary flywheel, (c) arc-shaped springs, (d) spring seats, (e) transmission flange, (f) plate, and (g) secondary flywheel.

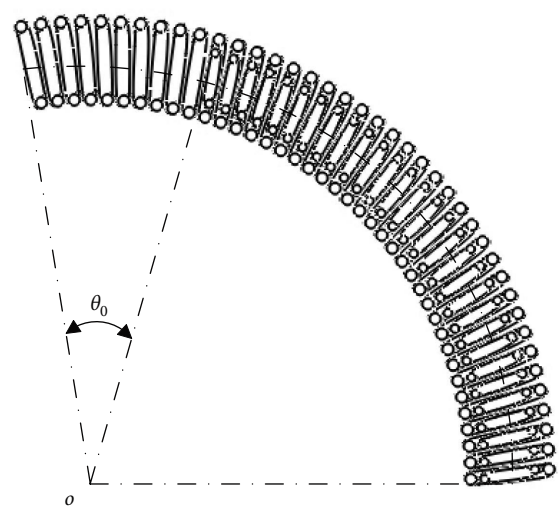

Figure 2: Schematic of the structure of the arc springs.

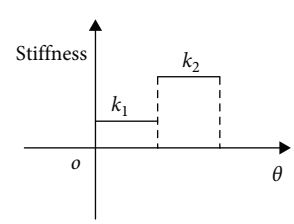

Figure 3: Piecewise linear stiffness characteristics.

3. Torsional Vibration Model of DMF

The DMF regulating characteristics of the fluctuation of the engine excitation can be analyzed based on the relative rotation angle θ of the primary and secondary flywheel.

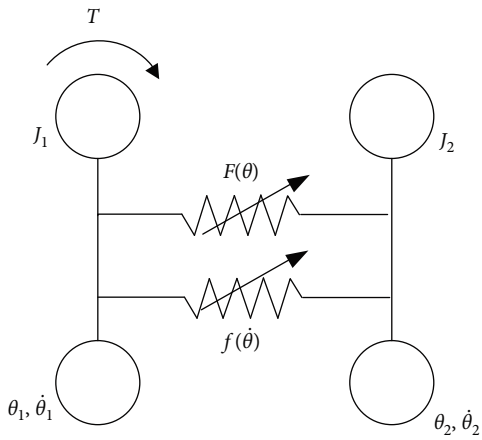

Figure 4: Simplified torsional vibration model of the DMF.

According to the structure and working principle of the DMF, it is simplified into a semidefinite torsional vibration system as shown in Figure 4.

In Figure 4, J_1—inertia of primary flywheel, J_2—inertia of secondary flywheel, $\theta_1, \dot{\theta}_1$—relative angular and angular velocity of primary flywheel, $\theta_2, \dot{\theta}_2$—relative angular and angular velocity of secondary flywheel, T—excitation torque, $F(\theta)$—function of the nonlinear torsional elastic force, and $f(\dot{\theta})$—function of nonlinear damping force.

According to Figure 4 and Newton's second law, the nonlinear differential equation of torsional vibration of the DMF is obtained as follows:

$$\begin{cases} J_1\ddot{\theta}_1 + f(\dot{\theta}) + F(\theta) = T\sin \upsilon t \\ J_2\ddot{\theta}_2 - f(\dot{\theta}) - F(\theta) = 0 \end{cases}, \tag{1}$$

where υ—excitation frequency, t—time, $\theta, \dot{\theta}, \ddot{\theta}$—relative angular, angular velocity, and angular acceleration of the DMF.

In Figure 5, c_1—damping coefficient of external arc spring, c_3—damping coefficient of internal arc spring, c_2—parallel damping coefficient, $c_2 = c_1 + c_3$.

According to the characteristic curves of the piecewise linear stiffness shown in Figure 3, and considering the piecewise linear damping characteristics [21] of internal and external (while $\dot{\theta} > 0$) arc springs shown in Figure 5, the function of the nonlinear torsional elastic force $F(\theta)$ and nonlinear damping force $f(\dot{\theta})$ are expressed as follows:

$$F(\theta) = \begin{cases} k_1\theta & -\theta_0 \le \theta \le \theta_0 \\ k_2\theta + (k_1 - k_2)\theta_0 & \theta_0 \le \theta \\ k_2\theta - (k_1 - k_2)\theta_0 & \theta \le -\theta_0 \end{cases}, \tag{2}$$

$$f(\dot{\theta}) = \begin{cases} c_1\dot{\theta} & -\theta_0 \le \theta \le \theta_0 \\ c_2\dot{\theta} & \theta_0 \le \theta \\ c_2\dot{\theta} & \theta \le -\theta_0 \end{cases}. \tag{3}$$

Substituting $\theta = \theta_1 - \theta_2$ into Equation (1), and Equation (1) is transformed as follows:

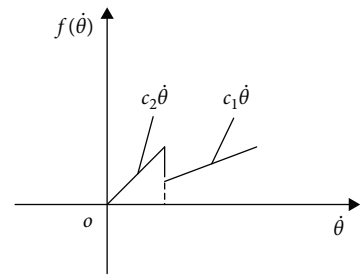

Figure 5: Function expression of nonlinear damping force.

$$J\ddot{\theta} + f(\dot{\theta}) + F(\theta) = T_0\sin \upsilon t, \tag{4}$$

where

$$J = J_1J_2/(J_1 + J_2), \tag{5}$$

$$T_0 = TJ_2/(J_1 + J_2). \tag{6}$$

4. Approximate Analytical Solution of Nonlinear Amplitude–Frequency Characteristics

In order to solve Equation (4), the average method by Chen [21] is used, and Equation (4) is transformed as follows:

$$F(\theta) = k_2\theta + h(\theta), \tag{7}$$

where

$$h(\theta) = \begin{cases} (k_1 - k_2)\theta & -\theta_0 \le \theta \le \theta_0 \\ (k_1 - k_2)\theta_0 & \theta_0 \le \theta \\ -(k_1 - k_2)\theta_0 & \theta \le -\theta_0 \end{cases}. \tag{8}$$

Substituting Equation (7) into Equation (4), and transforming the semidefinite torsional vibration system into a single-degree-of-freedom system, the nonlinear terms and excitation are multiplied by a small parameter ε, then the dynamic equation of the DMF are expressed as follows:

$$J\ddot{\theta} + k_2\theta = \varepsilon\left(T_0\sin \upsilon t - h(\theta) - f(\dot{\theta})\right). \tag{9}$$

Equation (9) is simplified as follows:

$$\ddot{\theta} + \omega^2\theta = \varepsilon\left(T_P\sin \upsilon t - g(\theta) - f(\dot{\theta})/J\right), \tag{10}$$

where

$$\omega = \sqrt{k_2/J}, \tag{11}$$

$$T_P = T_0/J, \tag{12}$$

$$g(\theta)=\begin{cases}(k_1-k_2)\theta/J & -\theta_0\le\theta\le\theta_0\\ (k_1-k_2)\theta_0/J & \theta_0\le\theta\\ -(k_1-k_2)\theta_0/J & \theta\le-\theta_0\end{cases}. \tag{13}$$

In order to study the resonance of ν approaching ω, assuming that

$$\omega-\upsilon=\varepsilon\sigma, \tag{14}$$

where σ—tuning parameter.

Assuming the first approximate solution of the system as follows:

$$\begin{cases}\theta=a\sin(\upsilon t+\varphi)\\ d\theta/dt=a\omega\cos(\upsilon t+\varphi)\end{cases}. \tag{15}$$

As shown in Equation (15), a, θ are functions of t. According to the average method, Equation (15) is transformed into a standard equation as follows:

$$\begin{cases}\dfrac{da}{dt}=-\dfrac{\varepsilon}{\omega}[g(a\sin\psi)+f(a\upsilon\cos\psi)/J-T_{\mathrm{P}}\sin\upsilon t]\cos\psi\\ \dfrac{d\varphi}{dt}=\omega-\upsilon+\dfrac{\varepsilon}{a\omega}[g(a\sin\psi)+f(a\upsilon\cos\psi)/J-T_{\mathrm{P}}\sin\upsilon t]\sin\psi\end{cases}, \tag{16}$$

where

$$\psi=\upsilon t+\varphi. \tag{17}$$

Equation (16) shows that the derivatives of a and θ are proportional to ε, so they are functions of changing slowly. The first approximation KB [21] transformation is used, and y and ϑ are introduced as new variables.

$$\begin{cases}a=y+\varepsilon U(t,y,\vartheta)\\ \varphi=\vartheta+\varepsilon V(t,y,\vartheta)\end{cases}. \tag{18}$$

And the derivatives of y and ϑ are as follows:

$$\begin{cases}dy/dt=\varepsilon Y_1(y)+\varepsilon^2Y^*(t,y,\vartheta,\varepsilon)\\ d\vartheta/dt=\varepsilon Z_1(y)+\varepsilon^2Z^*(t,y,\vartheta,\varepsilon)\end{cases}, \tag{19}$$

where Y_1, Z_1 do not contain t, and U, V, Y^*, Z^*, are ϑ's periodic functions with a period of 2π and a periodic function of t in Equation (19).

Substituting Equation (15) into Equation (16) and considering Equation (19), yields:

$$\begin{cases}\varepsilon Y_1+\varepsilon^2Y^*+\varepsilon\dfrac{\partial U}{\partial t}+\varepsilon\dfrac{\partial U}{\partial y}(\varepsilon Y_1+\varepsilon^2Y^*)+\varepsilon\dfrac{\partial U}{\partial\vartheta}(\varepsilon Z_1+\varepsilon^2Z^*)=\varepsilon F_1+\varepsilon^2\cdots\\ \varepsilon Z_1+\varepsilon^2Z^*+\varepsilon\dfrac{\partial V}{\partial t}+\varepsilon\dfrac{\partial V}{\partial y}(\varepsilon Y_1+\varepsilon^2Y^*)+\varepsilon\dfrac{\partial V}{\partial\vartheta}(\varepsilon Z_1+\varepsilon^2Z^*)=\varepsilon F_2+\varepsilon^2\cdots\end{cases}, \tag{20}$$

where

$$\begin{cases}F_1=-\dfrac{1}{\omega}[g(y\sin\psi)+f(y\upsilon\cos\psi)/J-T_{\mathrm{P}}\sin\upsilon t]\cos\psi\\ F_2=\omega-\upsilon+\dfrac{1}{y\omega}[g(y\sin\psi)+f(y\upsilon\cos\psi)/J-T_{\mathrm{P}}\sin\upsilon t]\sin\psi\end{cases}. \tag{21}$$

Making the coefficients of the first term of ε at both ends of Equation (20) equal, we obtain:

$$\begin{cases}Y_1+\partial U/\partial t=F_1\\ Z_1+\partial V/\partial t=F_2\end{cases}. \tag{22}$$

In order to satisfy the condition that Y_1 and Z_1 do not contain t, we obtain:

$$\begin{cases}Y_1=\dfrac{1}{2\pi}\displaystyle\int_0^{2\pi}F_1d\psi=-\dfrac{1}{2\pi\omega}\int_0^{2\pi}f(y\upsilon\cos\psi)\cos\psi d\psi/J-\dfrac{T_{\mathrm{P}}}{\omega+\upsilon}\sin\varphi\\ Z_1=\omega-\upsilon+\dfrac{1}{2\pi\omega y}\displaystyle\int_0^{2\pi}g(y\sin\psi)\sin\psi d\psi-\dfrac{T_{\mathrm{P}}}{y(\omega+\upsilon)}\cos\varphi\end{cases}. \tag{23}$$

The approximation relation of $2\omega\approx\omega+\upsilon$ is applied in Equation (23), and only the first term of ε is taken into account in Equation (19), and substituting Y_1 and Z_1 into Equation (19), we obtain:

$$\begin{cases}\dfrac{dy}{dt}=-\dfrac{\varepsilon}{2\pi\omega}\displaystyle\int_0^{2\pi}f(y\upsilon\cos\psi)\cos\psi d\psi/J-\dfrac{\varepsilon T_{\mathrm{P}}}{\omega+\upsilon}\sin\varphi\\ \dfrac{d\vartheta}{dt}=\omega-\upsilon+\dfrac{\varepsilon}{2\pi\omega y}\displaystyle\int_0^{2\pi}g(y\sin\psi)\sin\psi d\psi-\dfrac{\varepsilon T_{\mathrm{P}}}{y(\omega+\upsilon)}\cos\varphi\end{cases}. \tag{24}$$

In order to get the integral of Equation (24), θ is substituted into Equation (13), and the corresponding integral bounds are given as follows:

$$g(y\sin\psi)=\begin{cases}\left(\frac{k_1}{J}-\frac{k_2}{J}\right)y\sin\psi & 0\le\psi\le\psi_0\\ \left(\frac{k_1}{J}-\frac{k_2}{J}\right)y\sin\psi_0 & \psi_0\le\psi\le\pi-\psi_0\\ \left(\frac{k_1}{J}-\frac{k_2}{J}\right)y\sin\psi & \pi-\psi_0\le\psi\le\pi\end{cases}, \tag{25}$$

$$f(y\upsilon\cos\psi)=\begin{cases}c_1y\upsilon\cos\psi & 0\le\psi\le\psi_0\\ c_2y\upsilon\cos\psi & \psi_0\le\psi\le\pi-\psi_0\\ c_1y\upsilon\cos\psi & \pi-\psi_0\le\psi\le\pi\end{cases}, \tag{26}$$

where

$$\psi_0=\arcsin(\theta_0/y). \tag{27}$$

The equivalent linear attenuation index $\delta_e(y)$ is given as follows:

$$\delta_e(y)=\frac{1}{\pi\omega y}\int_0^{\pi}f(y\upsilon\cos\psi)\cos\psi d\psi/J=\frac{c_2}{2J}(1+\chi(\alpha,Z)), \tag{28}$$

where

$$\chi(\alpha,Z)=\frac{2(\alpha-1)}{\pi Z}\left(Z\arcsin\frac{1}{Z}+\sqrt{1-\frac{1}{Z^2}}\right), \tag{29}$$

$$\alpha=c_1/c_2, Z=y/\theta_0. \tag{30}$$

The equivalent linear natural frequency $\omega_e(y)$ (backbone curve equation) is given as follows:

$$\omega_e(y)=\omega+\frac{1}{\pi\omega y}\int_0^{\pi}g(y\sin\psi)\sin\psi d\psi=\omega+\frac{k_2}{2\omega J}\chi(\beta,Z), \tag{31}$$

where

$$\chi(\beta,Z)=\frac{2(\beta-1)}{\pi Z}\left(Z\arcsin\frac{1}{Z}+\sqrt{1-\frac{1}{Z^2}}\right), \tag{32}$$

$$\beta=k_1/k_2. \tag{33}$$

Substituting Equations (28) and (31) into Equation (24), we obtain:

Table 1: Basic parameters.

Parameter	Value
J_1	0.17 kg·m^2
J_2	0.15 kg·m^2
k_1	6 N·m/(degree)
k_3	14 N·m/(degree)
c_1	0.06 N·ms/(rad)
c_3	0.08 N·ms/(rad)
θ_0	18°

$$\begin{cases}\frac{dy}{dt}=-\varepsilon\left(\delta_e(y)+\frac{T_P}{\omega+\upsilon}\sin\varphi\right)\\ \frac{d\vartheta}{dt}=\varepsilon(\omega_e(y)-\upsilon)-\frac{\varepsilon T_P}{y(\omega+\upsilon)}\cos\varphi\end{cases}. \tag{34}$$

The approximation relation of $\omega+\upsilon\approx 2\upsilon$ is applied in the first equation of Equation (34), and making Equation (34) equal to zero, then the expression of υ is obtained as follows:

$$\upsilon=\sqrt{\omega_e^2(y)-2\delta_e^2(y)\pm\sqrt{(\omega_e^2(y)-2\delta_e^2(y))^2-(\omega_e^4(y)-\lambda^2)}}, \tag{35}$$

where

$$\lambda=T_P/y. \tag{36}$$

5. Calculation and Analysis of DMF

5.1. Analysis of Amplitude–Frequency Response Characteristics. Table 1 presents the basic parameters of the nested arc-shaped short spring DMF with spring seats which have the function of overload protection.

The amplitude–frequency characteristic curve of DMF is shown in Figure 6, which is obtained by taking the parameters shown in Table 1 into Equation (35) and under the excitation torque $T=60$ N·m. In Figure 6, the solid line represents the steady response, the dashed line represents the unsteady response, and the dotted line represents the backbone curve.

Equation (31) shows that the relationship between the equivalent natural frequency $\omega_e(y)$ and the relative angular θ is nonlinear. It can be seen from Figure 6 that the backbone curve and the amplitude–frequency characteristic curve appear with the inflection point at θ_0, and the amplitude–frequency response curve bends to the right and jumps with the excitation frequency ν changing slowly.

The amplitude of the relative angular θ gradually increases along the amplitude–frequency characteristic curve from Point A to Point B, and to Point C, with the excitation frequency ν changing slowly from low to high, then reaches Point D. The amplitude will suddenly jump from Point D to Point E if the excitation frequency ν continues to increase,

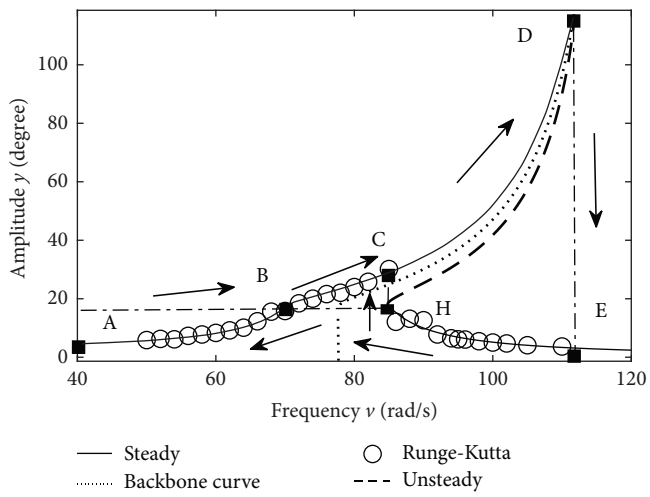

FIGURE 6: Amplitude–frequency characteristic curve of DMF.

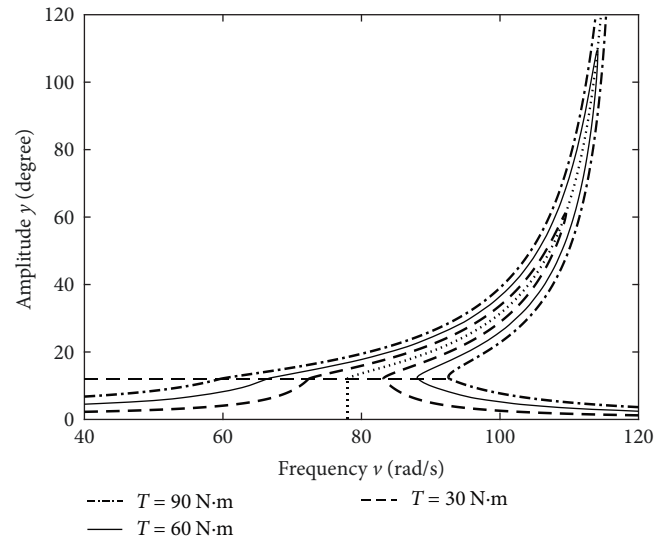

FIGURE 7: Amplitude–frequency response curves of different T.

then decrease gradually along the amplitude–frequency characteristic curve.

If the excitation frequency ν reduces slowly from high to low, the amplitude of the relative angular θ gradually increases along the amplitude–frequency characteristic curve from Point E to Point H. If the excitation frequency ν reduces continuously, the amplitude will suddenly jump from Point H to Point C and then decreases along the direction from Point B to Point A.

According to the amplitude–frequency characteristic curve of DMF, there are jumping and lagging phenomena which lead to the instability of the system such as DH segment of the curve, with the excitation frequency ν changing continuously and slowly.

To verify the accuracy of the analytical solution, the R–K method is used to calculate the frequency response characteristics of the DMF. The results are shown in Figure 6. In Figure 6, "o" denotes the frequency response result obtained by the frequency reducing slowly from high to low. It can be seen from Figure 6 that the numerical calculation results are consistent with the analytical solutions, which shows that it is feasible to analyze the amplitude–frequency characteristics of the DMF by means of average method.

5.1.1. Effect of Excitation Torque on Amplitude–Frequency Characteristics. The amplitude–frequency characteristics of the DMF are studied and obtained as shown in Figure 7, under different excitation values such as $T = 30\,\text{N·m}$, $T = 60\,\text{N·m}$, and $T = 90\,\text{N·m}$. Figure 7 shows that the backbone curve does not change, and the corresponding response amplitude in the steady range increases at the same frequency, and the resonant frequency band becomes wider and the peak of resonant amplitude becomes larger, with the increase of excitation torque.

5.1.2. Effect of Inertia on Amplitude–Frequency Characteristics. The amplitude–frequency response curves corresponding to different inertia of the primary flywheel such as $J_1 = 0.16\,\text{kg·m}^2$, $J_1 = 0.36\,\text{kg·m}^2$, and $J_1 = 0.56\,\text{kg·m}^2$ are obtained, as shown in Figure 8.

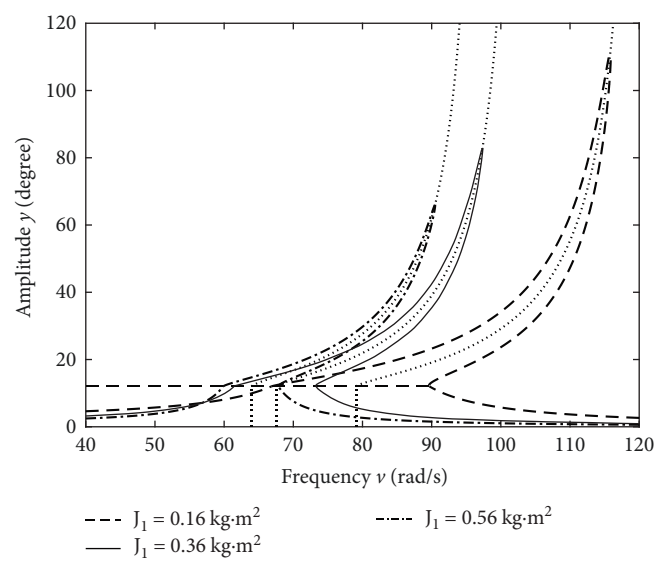

FIGURE 8: Amplitude–frequency response curves of different J_1.

It can be seen from Figure 8 that the backbone curve and the amplitude–frequency characteristic curves are shifted to the left and the inflection bends to the left simultaneously, the peak of resonant amplitude is reduced, and the resonant frequency band is narrowed, with the increase of J_1.

The amplitude–frequency response curves corresponding to different inertia of the secondary flywheel such as $J_2 = 0.08\,\text{kg·m}^2$, $J_2 = 0.13\,\text{kg·m}^2$, and $J_2 = 0.18\,\text{kg·m}^2$ are obtained, as shown in Figure 9.

It can be seen from Figure 9 that the backbone curve and the amplitude–frequency characteristic curves are shifted to the left and the inflection bends to the left simultaneously, the peak of resonant amplitude is increased, and the resonant frequency band is widened, with the increase of J_2.

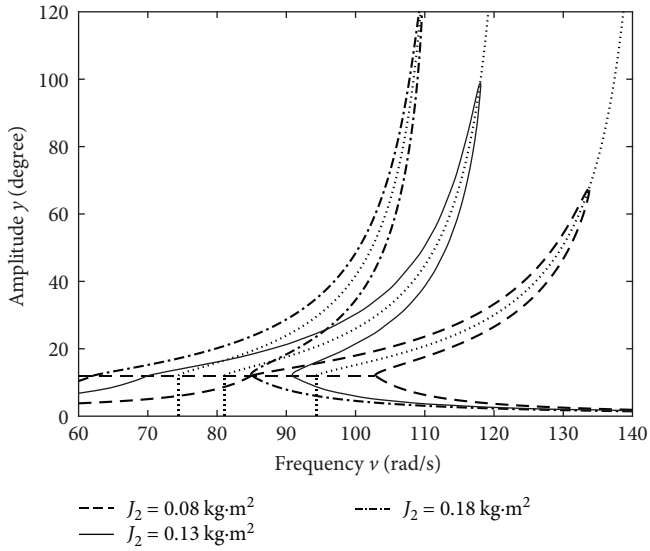

Figure 9: Amplitude–frequency response curves of different J_2.

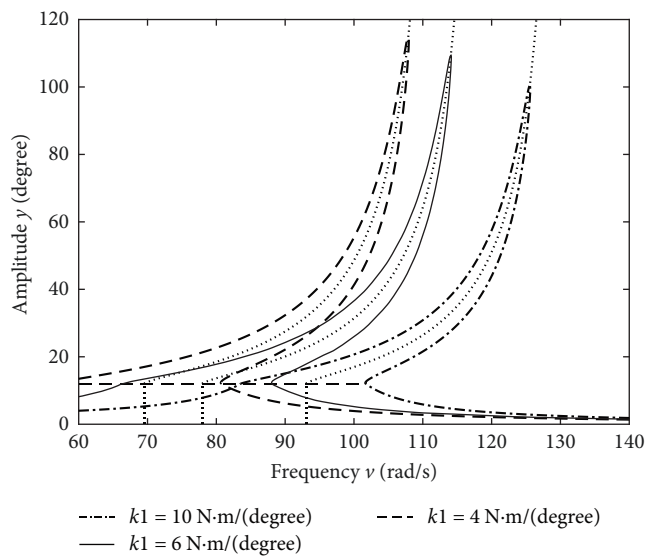

Figure 10: Amplitude–frequency response curves of different k_1.

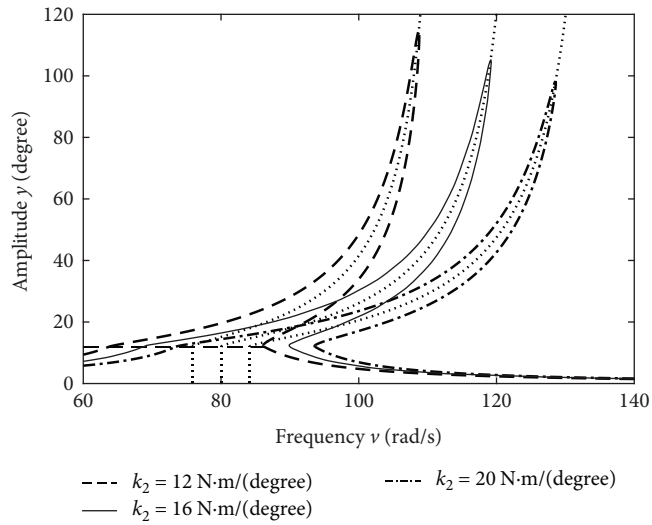

Figure 11: Amplitude–frequency response curves of different k_2.

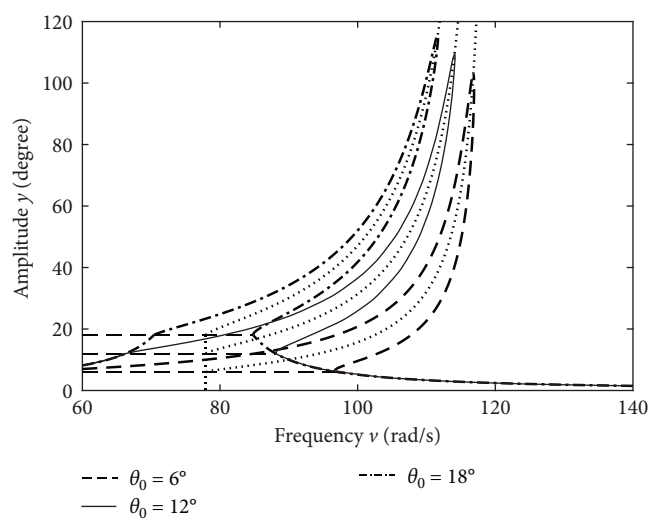

Figure 12: Amplitude–frequency response curves of different θ_0.

5.1.3. Effect of Torsional Stiffness on Amplitude–Frequency Characteristics. The amplitude–frequency response curves corresponding to different first-stage stiffness such as $k_1 = 4$ N·m/(degree), $k_1 = 6$ N·m/(degree), and $k_1 = 10$ N·m/(degree) are obtained, as shown in Figure 10.

It can be seen from Figure 10 that the backbone curve and the amplitude–frequency characteristic curves are shifted to the right, and the inflection bends to the right simultaneously (the bending to the right is not obvious), the peak of resonant amplitude is reduced but not obviously, and the resonant frequency band is narrowed, with the increase of k_1.

The amplitude–frequency response curves corresponding to different second-stage stiffness such as $k_2 = 12$ N·m/(degree), $k_2 = 16$ N·m/(degree), and $k_2 = 20$ N·m/(degree) are obtained, as shown in Figure 11.

It can be seen from Figure 11 that the backbone curve and the amplitude–frequency characteristic curves are shifted to the right and the inflection bends to the right simultaneously (the bending to the right is not obvious) with the increase of k_2, and the peak of resonant amplitude is reduced, but the resonant frequency band changing is not obvious.

5.1.4. Effect of Angular Clearance on Amplitude–Frequency Characteristics. The amplitude–frequency response curves corresponding to different angular clearances such as $\theta_0 = 6°$, $\theta_0 = 12°$, and $\theta_0 = 18°$ are obtained, as shown in Figure 12. It can be seen from Figure 12 that the resonant frequency band becomes narrow, but the influence on the peak of the resonant amplitude is not obvious, with the increase of θ_0.

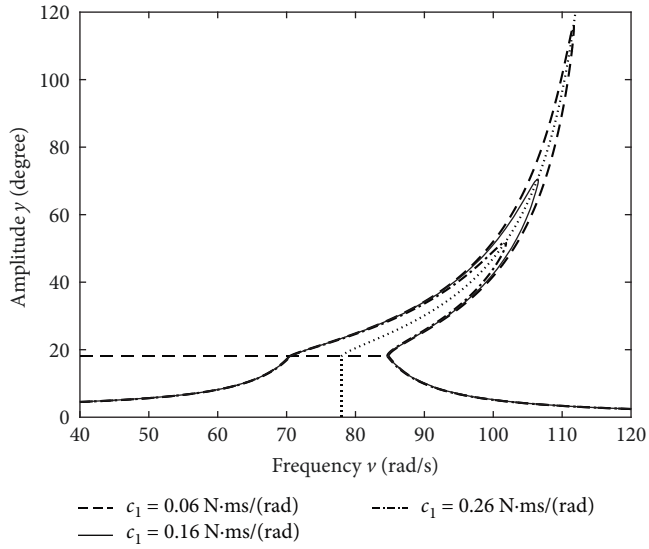

FIGURE 13: Amplitude–frequency response curves of different c_1.

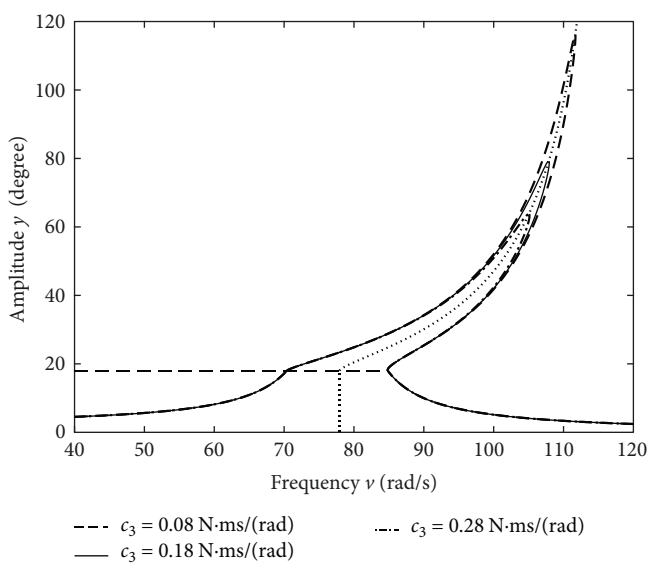

FIGURE 14: Amplitude–frequency response curves of different c_3.

5.1.5. Effect of Piecewise Damping on Amplitude–Frequency Characteristics. The amplitude–frequency response curves corresponding to damping coefficient of external arc spring such as $c_1 = 0.06$ N·ms/(rad), $c_1 = 0.16$ N·ms/(rad), and $c_1 = 0.26$ N·ms/(rad) are obtained, as shown in Figure 13. It can be seen from Figure 13 that the peak of resonant amplitude is reduced obviously and the unstable region becomes smaller with the increase of c_1.

The amplitude–frequency response curves corresponding to damping coefficient of internal arc spring such as $c_3 = 0.08$ N·ms/(rad), $c_3 = 0.18$ N·ms/(rad), and $c_3 = 0.28$ N·ms/(rad) are obtained, as shown in Figure 14. It can be seen from Figure 14 that the peak of resonant amplitude is reduced obviously and the unstable region becomes smaller with the increase of c_3, which is similar to that of c_1.

5.2. Analysis of Nonlinear Forced Vibration Response. The nonlinear forced vibration response of the DMF system is analyzed by taking the excitation frequencies of $\nu = 30$ rad/s, $\nu = 80$ rad/s, $\nu = 100$ rad/s, and $\nu = 140$ rad/s, respectively.

The time domain angular displacement and frequency spectrum and phase trajectory and Poincaré section are analyzed under the excitation frequency of $\nu = 30$ rad/s and shown in Figure 15. The system response consists of superharmonic forced vibration under the frequencies of 62.89 rad/s $\approx 2\nu$ and 188.7 rad/s $\approx 6\nu$. The phase trajectory is a closed loop and the Poincaré Section 1 point, there is a period 1 motion while θ varying with t.

The time domain angular displacement and frequency spectrum and phase trajectory and Poincaré section are analyzed under the excitation frequency of $\nu = 80$ rad/s and shown in Figure 16. The system response consists of a steady-state forced vibration under the frequency of 79.77 rad/s $\approx \nu$ and vibrations under the frequency of 62.38 rad/s, amplitude of 15.64° and frequency of 46.02 rad/s, amplitude of 2.121°. The phase trajectories are superposed ellipses, and the points on the Poincaré section can form a closed loop, there is a quasi-periodic motion while θ varying with t.

The time domain angular displacement and frequency spectrum and phase trajectory and Poincaré section are analzsed under the excitation frequency of $\nu = 100$ rad/s and shown in Figure 17. The system response consists of vibrations under the frequency of 56.76 rad/s, amplitude of 5.098° and frequency of 62.89 rad/s, amplitude of 40.33°, and frequency of 69.03 rad/s, amplitude of 23.91°. The phase trajectories are superimposed approximate ellipses with diffusing outwards, and the points on the Poincaré section can not form a closed loop, there is a chaotic motion while θ varying with t.

The time domain angular displacement and frequency spectrum and phase trajectory and Poincaré section are analyzed under the excitation frequency of $\nu = 140$ rad/s and shown in Figure 18. The system response consists of vibrations under the frequency of 29.66 rad/s, amplitude of 4.261° and frequency of 62.38 rad/s, amplitude of 2.481°. The phase trajectories are superimposed approximate ellipses with diffusing outwards, and the points on the Poincaré section can form a closed loop, there is a quasi-periodic motion while θ varying with t.

In summary, Figures 15–18 show the nonlinear forced vibration responses of the DMF system under different excitation frequencies. It can be seen that there are vibrations of periodic 1 motion, and quasi-periodic motion and chaotic motion while θ varying with t.

6. Conclusions

The nonlinear amplitude–frequency characteristics of the DMF system are solved by means of the average method, considering the nonlinear factors of the piecewise linear stiffness and damping of the DMF. The influences of the parameters of the DMF on the nonlinear amplitude–frequency characteristics and the forced vibration response under different excitation frequencies of the system are analyzed.

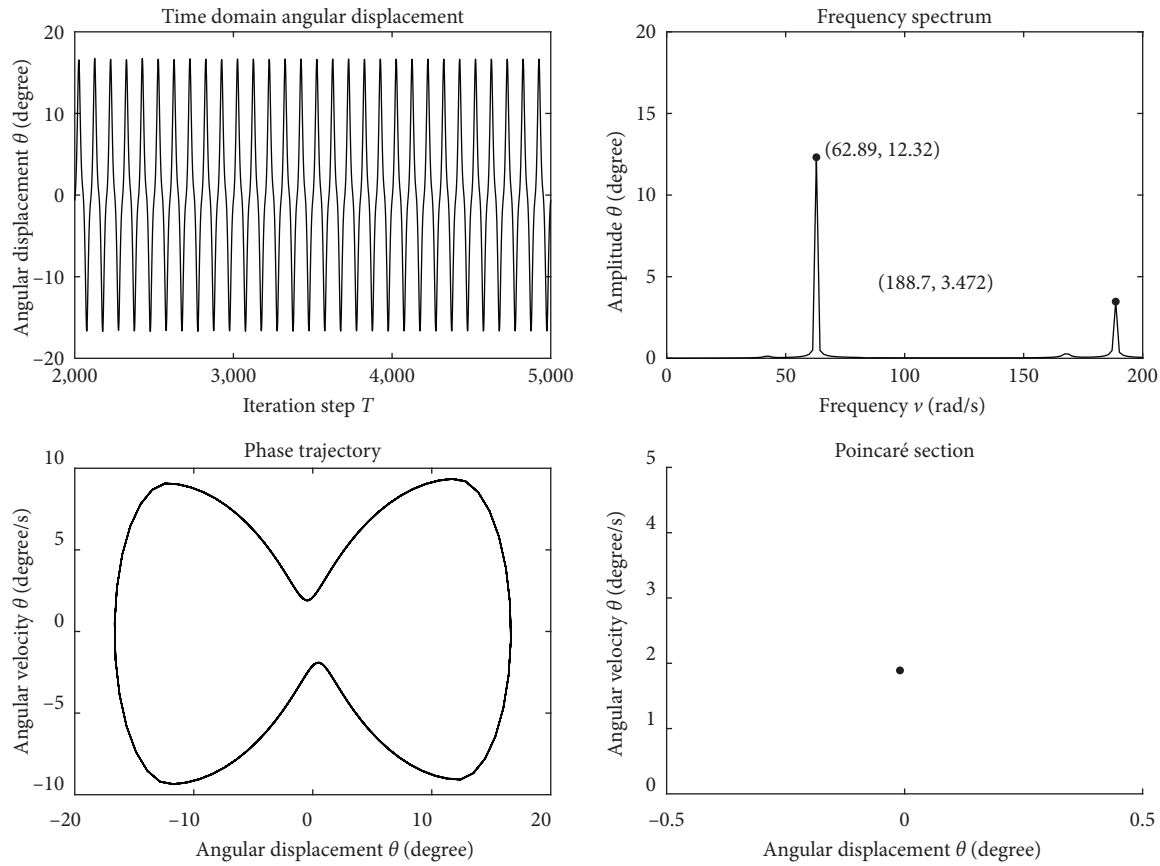

FIGURE 15: Time domain angular displacement, frequency spectrum, phase trajectory, and Poincaré section ($\nu = 30$ rad/s).

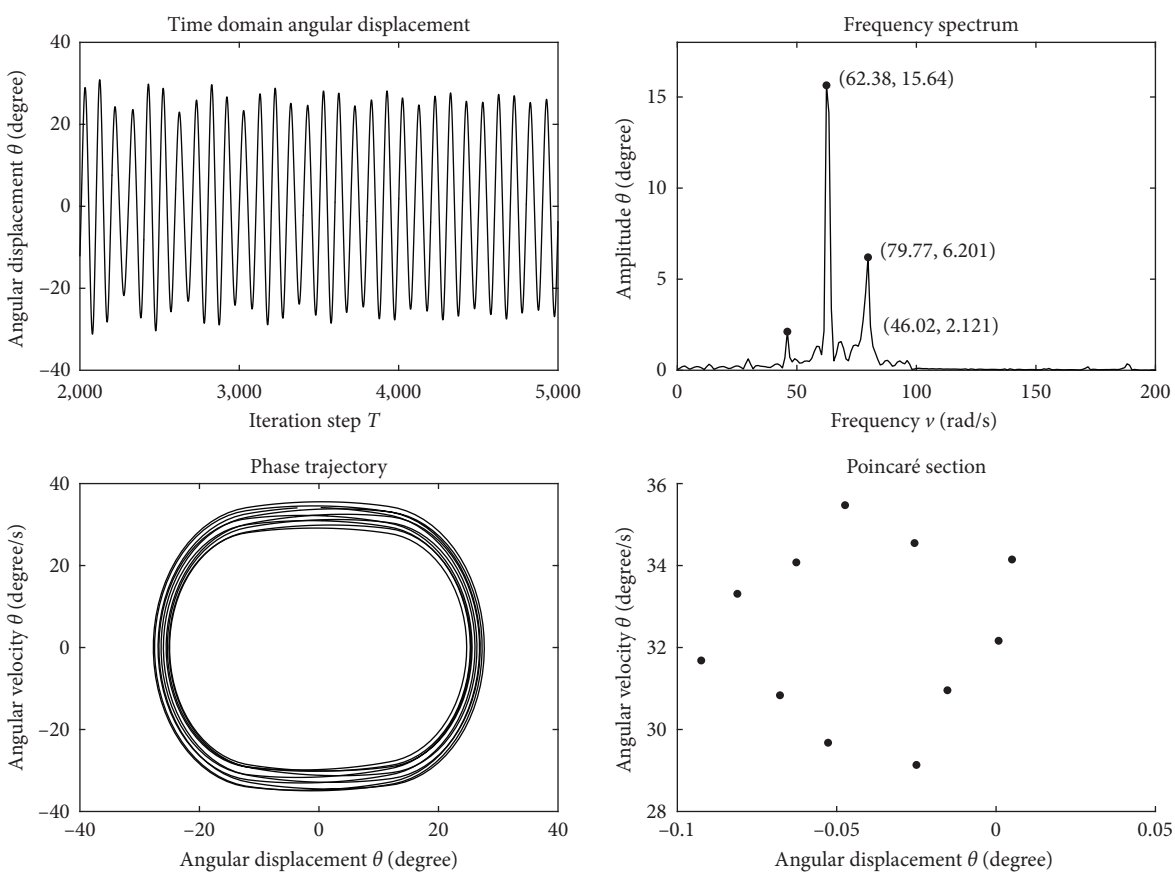

FIGURE 16: Time domain angular displacement, frequency spectrum, phase trajectory, and Poincaré section ($\nu = 80$ rad/s).

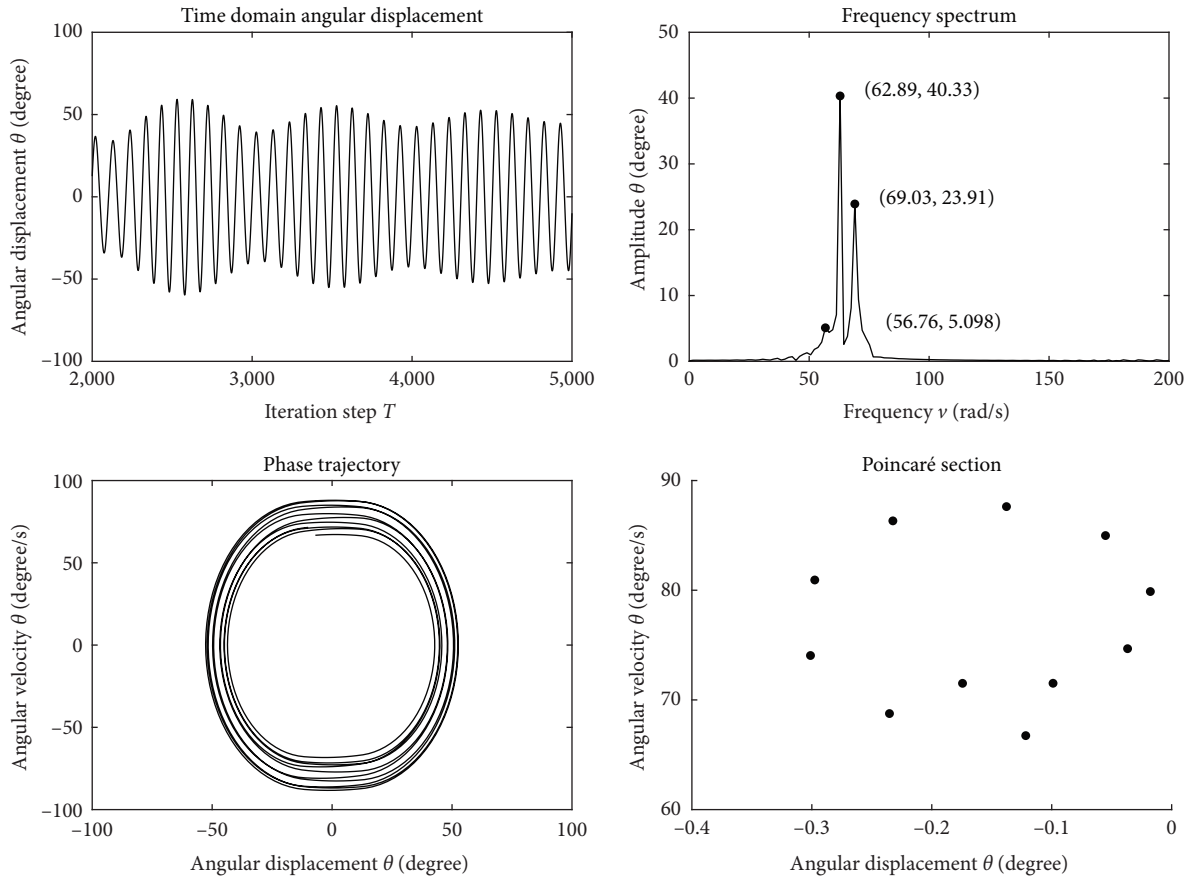

FIGURE 17: Time domain angular displacement, frequency spectrum, phase trajectory, and Poincaré section ($\nu = 100$ rad/s).

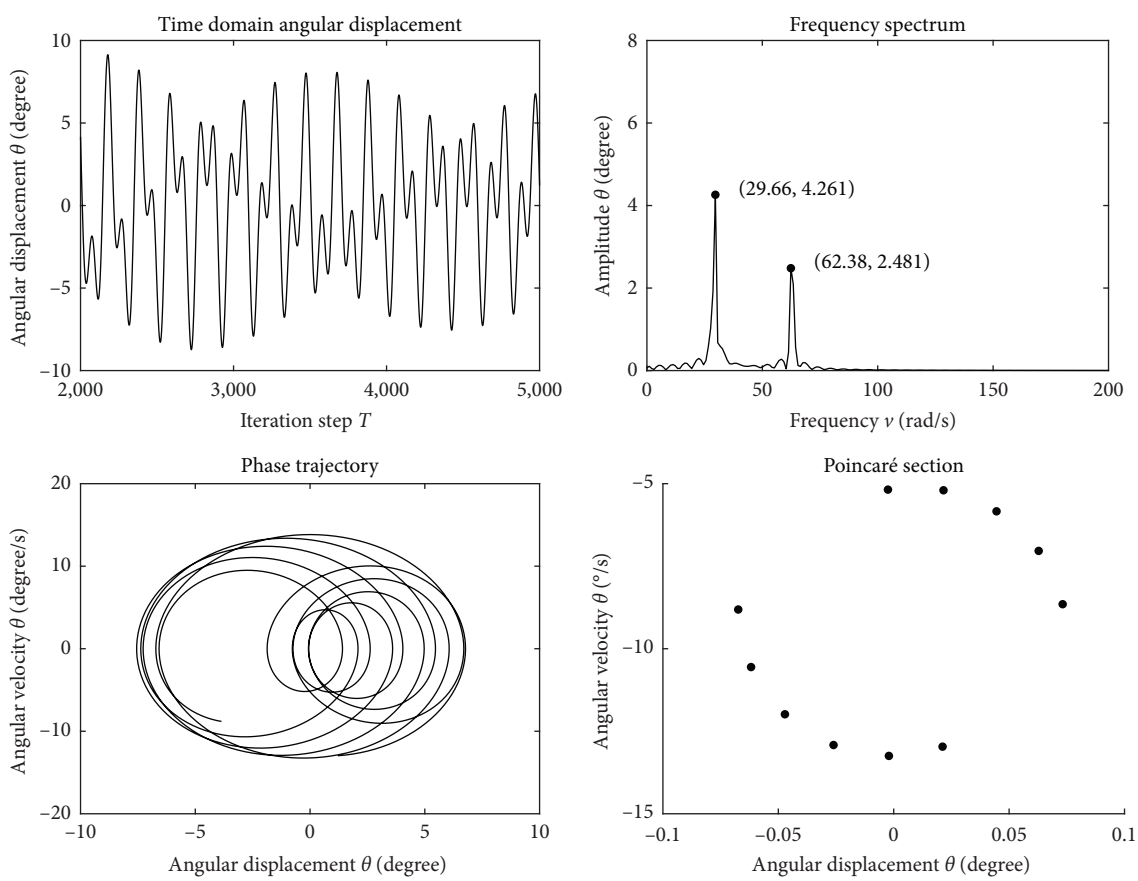

FIGURE 18: Time domain angular displacement, frequency spectrum, phase trajectory, and Poincaré section ($\nu = 140$ rad/s).

(1) The torsional vibration of the DMF system has obvious nonlinear characteristics due to the nonlinear factors, such as the amplitude–frequency characteristic curve bending and jumping with the changing of excitation frequency.
(2) The peak of resonant amplitude of the system can be obviously reduced by increasing the inertia of the primary flywheel and decreasing the inertia of the secondary flywheel. The primary flywheel inertia and the first-stage stiffness have obvious influence on the resonant frequency band of the system.
(3) The nonlinear forced vibration response of the system includes periodic 1 motion, quasi-periodic motion, and chaotic motion with the excitation frequency changing.
(4) The parameters of the DMF can be optimized by nonlinear amplitude–frequency analysis when the DMF structure is designed.

Data Availability

The data supporting the findings of this study are available from the corresponding author upon reasonable request.

Conflicts of Interest

The authors declare that they have no conflicts of interest.

Acknowledgments

This work is supported by the Key Scientific Research Projects of Colleges and Universities of Henan, China (Nos. 23B460007, 23B460003, and 24B460023), the National Natural Science Foundation of China (Nos. 51805167 and 52265011).

References

[1] S. Theodossiades, M. Gnanakumarr, H. Rahnejat, and P. Kelly, "Effect of a dual-mass flywheel on the impact-induced noise in vehicular powertrain systems," *Proceedings of the Institution of Mechanical Engineers, Part D: Journal of Automobile Engineering*, vol. 220, no. 6, pp. 747–761, 2006.
[2] T.-S. Kang, S. K. Kauh, and K.-P. Ha, "Development of the displacement measuring system for a dual mass flywheel in a vehicle," *Proceedings of the Institution of Mechanical Engineers, Part D: Journal of Automobile Engineering*, vol. 223, no. 10, pp. 1273–1281, 2009.
[3] G. Zheng, C. Wang, and T. Hao, "Influence of dual mass flywheel on NVH performance of powertrains," *Journal of Chongqing University of Technology (Natural Science)*, vol. 32, no. 5, pp. 57–61, 2018.
[4] L. Wramner, "Torsional vibrations in heavy-duty truck powertrains with dual mass flywheels," *International Journal of Heavy Vehicle Systems*, vol. 28, no. 5, pp. 585–611, 2021.
[5] S. Liu, "Influences of a dual-mass flywheel damper on idling vibration," *Transactions of the Chinese Society for Agricultural Machinery*, vol. 35, no. 3, pp. 16–19, 2004.
[6] L. Song, H. Niu, L. Zeng, and H. Tian, "A study on the modeling and torsional vibration attenuation for vehicle powertrain system based on unit analysis," *Automotive Engineering*, vol. 37, no. 8, pp. 866–874, 2015.
[7] G. Hou, Y. Xu, Y. Zhang, and X. Cheng, "Optimized design of dual-mass flywheel to improve booming vibration and shift-shock," *Noise and Vibration Control*, vol. 42, no. 2, pp. 253–257, 2022.
[8] L. Chen, R. Zeng, and Z. Jiang, "Nonlinear dynamical model of an automotive dual mass flywheel," *Advances in Mechanical Engineering*, vol. 7, no. 6, pp. 1267–1276, 2015.
[9] Y. Wang, X. Qin, S. Huang, and S. Deng, "Design and analysis of a multi-stage torsional stiffness dual mass flywheel based on vibration control," *Applied Acoustics*, vol. 104, pp. 172–181, 2016.
[10] Z. Xia, S. Chen, L. He, and H. Wu, "Study on parameter matching of circumferential short spring dual-mass flywheel," *Journal of Guangxi University (Natural Science Edition)*, vol. 44, no. 3, pp. 599–605, 2019.
[11] W. Shi, L. Chen, Z. Chen, and J. Ding, "A research on nonlinear vibration characteristics of piecewise stiffness dual mass flywheel," *Automotive Engineering*, vol. 41, no. 4, pp. 417–425, 2019.
[12] W. Shi, L. Chen, G. Zhang, and Z. Chen, "Modeling and tests for torsional characteristics of multi-stage stiffness dual mass flywheel torsional dampers," *Journal of Jilin University (Engineering and Technology Edition)*, vol. 50, no. 1, pp. 44–52, 2020.
[13] Z. Jiang and L. Chen, "Study on the design method of circumferential arc spring dual mass flywheel," *Chinese Internal Combustion Engine Engineering*, vol. 30, no. 6, pp. 31–36, 2009.
[14] L. Song, J. Zhou, R. Wu et al., "Research and application on design theory of friction dual mass flywheel with double-stage piecewise variable stiffness," *Journal of Mechanical Engineering*, vol. 48, no. 15, pp. 150–157, 2012.
[15] C. Long, W. Shi, and Z. Chen, "Research on dynamic behavior of torsional absorber in powertrain system considering nonlinear factors," *Journal of Vibration and Control*, vol. 27, no. 13-14, pp. 1656–1667, 2021.
[16] L. Zeng, Q. Chen, and L. Song, "Nonlinear vibration of a dual mass flywheel considering the friction torque and clearance variation characteristics of the stiffness of damping spring," *Journal of Vibration and Shock*, vol. 37, no. 6, pp. 231–237, 2018.
[17] L. Zeng, Q. Chen, X. Yuan, Q. Xiao, C. Zhou, and J. Huang, "Study on nonlinear vibration of vehicle dual mass flywheels with three-stage piecewise stiffnesses," *China Mechanical Engineering*, vol. 29, no. 20, pp. 2453–2459, 2018.
[18] S. Wang, L. Hua, C. Yang, Y. Zhang, and X. Tan, "Nonlinear vibrations of a piecewise-linear quarter-car truck model by incremental harmonic balance method," *Nonlinear Dynamics*, vol. 92, no. 4, pp. 1719–1732, 2018.
[19] D. Shao, Z. Lu, and L. Chen, "Power flow characteristics of a two-stage nonlinear vibration isolation system," *Journal of Vibration Engineering*, vol. 30, no. 5, pp. 764–773, 2017.
[20] Z. Ruan, H. Xing, and X. Lu, "Dynamic characteristic analysis of a piecewise damping vibration isolation system," *Journal of Dynamics and Control*, vol. 21, no. 5, pp. 44–52, 2023.
[21] Y. Chen, *Nonlinear Vibration*, pp. 117–140, Tianjin Science and Technology Press, Tianjin, China, 1983.